Baseline Desensitizing In Translation Averaging

Bingbing Zhuang, Loong-Fah Cheong, Gim Hee Lee
National University of Singapore
zhuang.bingbing@u.nus.edu, {eleclf,gimhee.lee}@nus.edu.sg

Abstract

Many existing translation averaging algorithms are either sensitive to disparate camera baselines and have to rely on extensive preprocessing to improve the observed Epipolar Geometry graph, or if they are robust against disparate camera baselines, require complicated optimization to minimize the highly nonlinear angular error objective. In this paper, we carefully design a simple yet effective bilinear objective function, introducing a variable to perform the requisite normalization. The objective function enjoys the baseline-insensitive property of the angular error and yet is amenable to simple and efficient optimization by block coordinate descent, with good empirical performance. A rotation-assisted Iterative Reweighted Least Squares scheme is further put forth to help deal with outliers. We also contribute towards a better understanding of the behavior of two recent convex algorithms, LUD [20] and Shapefit/kick [9], clarifying the underlying subtle difference that leads to the performance gap. Finally, we demonstrate that our algorithm achieves overall superior accuracies in benchmark dataset compared to state-of-the-art methods, and is also several times faster.

1. Introduction

Modern large-scale Structure-from-Motion (SfM) systems have enjoyed widespread success in many applications [26, 33, 27, 21, 17]. Earlier methods often adopt an incremental method by adding the cameras one by one sequentially as the size of the model grows up. As a consequence, the quality of the result heavily depends on the order in which the cameras are added, and the accumulated error often leads to significant drift as the size of the model increases. Therefore, frequent intermediate bundle adjustments (BA) [29] have to be applied to obtain stable result, which unfortunately increases the computational cost substantially. Given such disadvantages, the global SfM method emerges as a serious alternative. Unlike the incremental method, the global method attempts to determine the absolute poses for all the cameras simultaneously from all the observed pairwise Epipolar Geometry (EG) [12]. Such a holistic approach spreads the error as uniformly as possible to the whole model, avoiding the problem of error accumulation and drift. Thus, BA needs to be run only once as a final refinement, leading to a more efficient system.

Formally, a global SfM algorithm takes as input a view graph $G{=}(V, E)$, where each node V_i in V and edge E_{ij} in E represent respectively a camera and relative pose $(\boldsymbol{R}_{ij}, \boldsymbol{t}_{ij})$ between the camera pair i and j whose fields of view overlap. It aims to find the absolute rotation $\boldsymbol{R}_i$ (a.k.a. rotation averaging) and location $\boldsymbol{t}_i$ (a.k.a. translation averaging) for each camera (up to a gauge freedom), such that the observed pairwise relative poses are best explained. In the noiseless case, the following two equations hold:

$$\boldsymbol{R}_i^T \boldsymbol{R}_j = \boldsymbol{R}_{ij}, \quad \frac{\boldsymbol{t}_j - \boldsymbol{t}_i}{||\boldsymbol{t}_j - \boldsymbol{t}_i||_2} = \boldsymbol{R}_i \boldsymbol{t}_{ij}. \tag{1}$$

Typically, rotation averaging is performed before translation averaging. In this paper, we follow this practice and shall focus on the second equation to perform translation averaging. Note that rotation is assumed to have been solved, and henceforth, for brevity, we shall denote $\boldsymbol{R}_i \boldsymbol{t}_{ij}$ as $\boldsymbol{v}_{ij}$.

Translation averaging is recognized as a hard task. One of the reasons is that the input relative translation estimate is sensitive to small camera baselines [7]. More importantly, EG only encodes the relative direction between cameras without any magnitude information. This causes a remove of the measurement space (directions between pairwise cameras) from the solution space (camera locations); this gap complicates the task much more, posing a significant challenge for the objective function design. The geometrically more meaningful objective would be to minimize the angular error between unit direction vectors [24, 32], but this leads to highly nonlinear functions that require complicated optimization. Instead, many recent methods simply ignore the normalization terms required for obtaining unit vectors, thereby yielding various forms of quasi-Euclidean distance terms in the objectives [16, 20, 9]. Often, such expediency allows the problem to be formulated as a convex optimization problem. However, the serious qualification of such magnitude-based objective functions is that they suffer from unbalanced weighting on each individual term when

the camera baselines are disparate in lengths, which may lead to biased solutions. These methods usually employ extensive preprocessing (e.g. outlier filtering) of the view graph to obtain better relative translations as input. This relieves but does not resolve the issue fundamentally and the accuracy is still limited in practice.

The contributions in this paper are threefold. (1) We show that by carefully designing the objective function, the numerical sensitivity of the solution to different camera baseline lengths can be readily removed. Specifically, we propose a return to the geometrically more meaningful, angular-error based objective function, putting forth a simple yet accurate Bilinear Angle-based Translation Averaging (BATA) framework. The key idea is to introduce a variable that performs the requisite normalization for a baseline-insensitive angular error term. This splits the original problem into easier subproblems, which can be easily optimized by block coordinate descent; empirically, the algorithm converges fast and yields superior performance. (2) To deal with outlier EG, we put forth a rotation-assisted Iterative Reweighted Least Squares (IRLS) scheme that leverages on the stable solution from rotation averaging as an extra source of information to determine the reliability of each observation in the view graph. (3) Our objective formulation also lends perspective to the behavior of various algorithms with a magnitude-based objective function [16, 20, 9]. We reveal that the subtle difference in the scale ambiguity removal strategy can nevertheless lead to rather different performance in such algorithms. Specifically, we build the equivalence between Shapefit/kick [9] and a slightly revised version of LUD [20], which allows us to trace the difference between Shapefit/kick and LUD to the scale ambiguity removal constraint. We then demonstrate that a weaker lower-bound constraint can cause a squashing effect on the overall shape of the recovered camera locations, especially under the presence of disparate baselines; conversely, a stronger constraint would help desensitize the effect of unbalanced baselines.

We demonstrate the utility of the proposed framework by extensive experiments on both synthetic and real data. In particular, we obtain superior performance on the benchmark 1DSfM dataset [32] both in terms of accuracy and efficiency compared to state-of-the-art methods. The code will be made publicly available.

2. Related Work

Rotation Averaging. Many methods exist for this task [11, 4, 15, 3, 8, 10]; we refer readers to [31] for a survey.

View Graph Preprocessing. Some methods [35, 32] utilize loop consistency to remove outlier EG in the view graph. Some other works attempt to refine the whole view graph using loop consistency [28, 23] or low-rank constraint [22]. A robust re-estimation of the pairwise translation after the recovery of absolute rotation is proposed in [20].

Translation Averaging. The pioneering work by Govindu [10] proposes to minimize the cross product between the relative camera location $\boldsymbol{t}_j - \boldsymbol{t}_i$ and the observed direction $\boldsymbol{v}_{ij}$. An ad-hoc iterative reweighting scheme is adopted to reduce the bias from different baseline lengths. As reported in [32], this generates poor accuracy in challenging dataset. Some methods aim to minimize the relaxation of the end-point distance $\left\|\boldsymbol{t}_j - \boldsymbol{t}_i - \|\boldsymbol{t}_j - \boldsymbol{t}_i\|_2 \boldsymbol{v}_{ij}\right\|_2^2$ or its variants. For example, Moulon et al. [16] propose to minimize a relaxed version using the L_∞ norm. A similar penalty is utilized in [20] but with a least unsquared deviations (LUD) form to be more robust. Goldstein et al. [9] propose a Shapefit/kick scheme based on the alternating direction method of multipliers (ADMM) to minimize the magnitude of the projection of $\boldsymbol{t}_j - \boldsymbol{t}_i$ on the orthogonal complement of $\boldsymbol{v}_{ij}$. Despite its convex formulation, works such as [16, 20, 9] suffer from bias due to the unnormalized camera baseline magnitude in their objectives, and often have to resort to extensive preprocessing strategies reviewed in the preceding paragraph to take more accurate EG view graph as input.

Works that minimize the angular residual between $\boldsymbol{t}_j - \boldsymbol{t}_i$ and $\boldsymbol{v}_{ij}$, denoted as θ_{ij}, are relatively rare in the literature. One of the representative works is that of Sim and Hartley [24]. They show that minimizing the maximal absolute value of $\tan\theta_{ij}$ from all observations, i.e. L_∞ norm, can be reformulated into a quasi-convex problem and a globally optimal solution can be found by solving a sequence of Second Order Cone Programming (SOCP) feasibility problems. However, it is well known that L_∞ is sensitive to outliers, and solving multiple SOCP problems restricts their method to medium-size problems. Wilson et al. [32] present another attempt by minimizing the residual of $\sin\theta_{ij}/2$. The trust-region method Levenberg-Marquard is applied to optimize the resultant highly nonlinear function. In our work, we present another objective function along this line of approach; it minimizes the residual of $\sin\theta_{ij}$ in essence, is easily optimizable and yet achieves superior performance.

Other heuristics have been proposed. These include coplanar constraint on triple cameras [13], reprojection error [14, 15], reducing the problem into similarity averaging by local depth estimation [6], and others [25, 5, 30, 19, 2]. We note that existing methods often include scene points to assist translation averaging and/or involve careful outlier filtering step. In this paper, we demonstrate the possibility of achieving good accuracy in practice even if we directly process the raw view graph. Such a concise framework is more amenable to efficient processing.

3. Method

3.1. Bilinear Angle-based Translation Averaging

Instead of penalizing the angular deviation θ_{ij} between

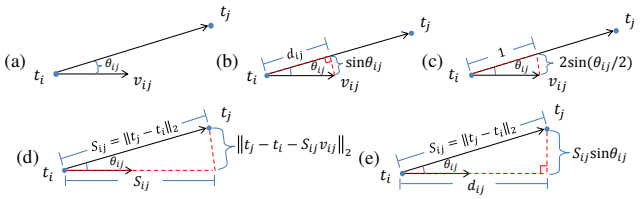

Figure 1: Geometric interpretation of the residuals penalized by different objective functions. (a) θ_{ij}. (b) BATA. (c) 1DSfM. (d) $\left\|\boldsymbol{t}_j-\boldsymbol{t}_i-\|\boldsymbol{t}_j-\boldsymbol{t}_i\|_2\boldsymbol{v}_{ij}\right\|_2$. (e) Shapefit/kick and RevisedLUD. Refer to the text for more details.

$\boldsymbol{t}_j-\boldsymbol{t}_i$ and the observed $\boldsymbol{v}_{ij}$ (illustrated in Fig. 1(a)) directly, many existing algorithms adopt an objective function of the form $\sum_{ij\in E}\left\|\boldsymbol{t}_j-\boldsymbol{t}_i-\|\boldsymbol{t}_j-\boldsymbol{t}_i\|_2\boldsymbol{v}_{ij}\right\|_2^2$ (Fig. 1(d)) or its variants. Note that this objective function is not normalized by the vector magnitude $\|\boldsymbol{t}_j-\boldsymbol{t}_i\|_2$, and is thus plagued by numerical difficulties when there is large variation in the magnitudes of $\boldsymbol{t}_j-\boldsymbol{t}_i$. In particular, though this objective will yield the true solution in the absence of noise, it is not necessarily statistically optimal under noisy condition. Let us illustrate this point via a toy example in the 2D plane. Referring to Fig. 2, suppose we know the ground-truth locations of three neighboring cameras to be at (-1, 0), (0, -1) and (5, 0) and would like to localize the fourth camera, with ground truth at (0, 0), according to its observed pairwise directions with respect to the three neighboring cameras. Due to noise, suppose all these observed directions deviate from their true direction by 3°. We use the red dot to denote the best location (found by exhaustive search on 2D grid) that minimizes the preceding magnitude-based residual. We also use the black star to denote the best location that minimizes the squared angular deviation $\sum_{ij\in E}\theta_{ij}^2$. Clearly, the solution in the former case is much worse off compared to that in the latter. In the former case, the objective function is essentially trying to determine the intersection point of the three direction vectors (in some least squares sense). This process is highly susceptible to errors when one or more cameras are far away. It follows that using such a magnitude-based objective function for the translation averaging problem would also experience similar sensitivity issue when there are disparate camera baseline distances.

In view of the foregoing discussion, we propose the following angle-based objective function instead:

$$\min_{\substack{\boldsymbol{t}_i, i\in V,\\ d_{ij}, ij\in E}} \quad \sum_{ij\in E}\rho(||(\boldsymbol{t}_j-\boldsymbol{t}_i)d_{ij}-\boldsymbol{v}_{ij}||_2), \tag{2}$$

$$s.t. \quad \sum_{i\in V}\boldsymbol{t}_i=0, \sum_{ij\in E}\langle \boldsymbol{t}_j-\boldsymbol{t}_i, \boldsymbol{v}_{ij}\rangle = 1,$$

$$d_{ij}\geq 0, \forall ij\in E,$$

where $\rho(\cdot)$ stands for a robust M-estimator function to be discussed in the next section. d_{ij} is a non-negative variable. The first two constraints on $\boldsymbol{t}$ are to remove the inherent positional and scale ambiguity. We now show that the optimal

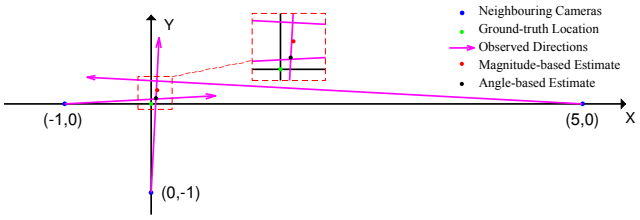

Figure 2: A toy example showing the sensitivity of different objectives to disparate baselines. See text for more explanations.

solution of this problem essentially minimizes an angular error $\sum_{ij\in E}\rho(h(\theta_{ij}))$, where

$$h(\theta_{ij}) = \begin{cases} \sin\theta_{ij}, & \theta_{ij}\leq 90°; \\ 1, & \theta_{ij} > 90°. \end{cases} \tag{3}$$

First, note that for any given candidate solution $\hat{\boldsymbol{t}}$, each d_{ij} serves to scale the relative location vector $\hat{\boldsymbol{t}}_j-\hat{\boldsymbol{t}}_i$ such that the Euclidean distance between the endpoint of $(\hat{\boldsymbol{t}}_j-\hat{\boldsymbol{t}}_i)d_{ij}$ and the unit vector $\boldsymbol{v}_{ij}$ is minimized. It follows that if the angle between $\hat{\boldsymbol{t}}_j-\hat{\boldsymbol{t}}_i$ and $\boldsymbol{v}_{ij}$ is less than 90°, the optimal value d_{ij} would be such that $(\hat{\boldsymbol{t}}_j-\hat{\boldsymbol{t}}_i)d_{ij}$ equals to the projection of $\boldsymbol{v}_{ij}$ onto the direction along $\hat{\boldsymbol{t}}_j-\hat{\boldsymbol{t}}_i$ and the penalty amounts to $\sin\theta_{ij}$ (Fig. 1(b)). The constraint $d_{ij}>0$ prevents d_{ij} from overcompensating when $\theta_{ij}>90°$, otherwise the objective would decrease when θ_{ij} increases from 90° to 180°. With this constraint, the optimal d_{ij} when $\theta_{ij}>90°$ would be 0 and the penalty would be 1.

As an alternative viewpoint, we could have regarded our objective function as a functional lifting and relaxation of the formulation in 1DSfM [32] which is an unconstrained minimization of the objective function $\sum_{ij\in E}\rho(\left\|(\boldsymbol{t}_j-\boldsymbol{t}_i)/\|\boldsymbol{t}_j-\boldsymbol{t}_i\|_2-\boldsymbol{v}_{ij}\right\|_2)$. The scale factor $1/\|\boldsymbol{t}_j-\boldsymbol{t}_i\|_2$ is replaced with the variable d_{ij} together with a relaxation of the constraint from $d_{ij}=1/\|\boldsymbol{t}_j-\boldsymbol{t}_i\|_2$ to $d_{ij}>0$. We note that since the scale factor in 1DSfM always normalizes the vector $\boldsymbol{t}_j-\boldsymbol{t}_i$ to a unit vector, its objective amounts to the penalty term $2\sin(\theta_{ij}/2)$ (Fig. 1(c)), which bears a close resemblance to the $\sin\theta_{ij}$ established in (3). It is clear that without any prior knowledge on the noise distribution, there is no reason for one to claim superiority over the other. Thus, while one can regard our objective function as a relaxation of that of 1DSfM, one should not see the relaxed version as a poorer cousin of the two, since there is nothing sacrosanct about $2\sin(\theta_{ij}/2)$ over $\sin\theta_{ij}$ in terms of its geometrical meaning. We also note that the relaxation reduces the original highly nonlinear term into a bilinear one that permits simple alternating optimization; compared to the solution of 1DSfM from Ceres [1], we empirically observe that BATA can generally recover the camera locations more reliably in real Internet photo collections, especially for those challenging sparsely connected cameras. Also note that our penalty term in (3) levels off after $\theta_{ij}>90°$, and this might bestow greater robustness to our formulation.

3.2. Robust Rotation-Assisted IRLS

As the estimated EG view graph often contains gross outliers, we thus embed the least squares objective into a M-estimator $\rho(\cdot)$. Iterative Reweighted Least Squares scheme is often used to optimize such objective, whereby a weighted least squares problem is solved in each iteration. The weight function, denoted as $\phi(\cdot)$ here, returns a value proportional to the goodness of fit of an observation ij, evaluated at the last iteration. Note that the specific form of $\phi(\cdot)$ depends on the M-estimator function $\rho(\cdot)$ being used, e.g. for Cauchy $\rho(\varepsilon)=log(1+\varepsilon^2/\alpha^2)$ and $\phi(\varepsilon)=\alpha^2/(\alpha^2+\varepsilon^2)$, where ε denotes the residual for each observation and α is the loss width. Since it is well known that rotation averaging can often be computed more reliably [11, 4], a natural idea is to leverage its result to assist the reliability assessment or weighting for each observed EG. We thus use for this purpose the following residual $\varepsilon = (\|(\boldsymbol{t}_j-\boldsymbol{t}_i)d_{ij}-\boldsymbol{v}_{ij}\|_2^2+\beta\|\boldsymbol{R}_i^T\boldsymbol{R}_j-\boldsymbol{R}_{ij}\|_2^2)^{1/2}$, whereby the goodness of fit of the rotation estimate also contributes to the weighting process. Here, β is a predefined weighting factor (set as 1 for all the experiments). It turns out that this strategy can generally improve the accuracy and speed up the convergence of BATA. For each IRLS iteration, we use Block Coordinate Descent (BCD) to optimize $\boldsymbol{t}$ and d, as summarized in Algo. 1.

Algorithm 1 IRLS-BCD solver

Input: View Graph $G=(V,E)$, Rotation Averaging Result.
Output: Camera Locations $\boldsymbol{t}_i, \forall i \in V$.

```
Initialize t_i, ∀i ∈ V, W_ij, ∀ij ∈ E; Set n = 0;
while n < IRLSIter AND not converged do
    m = 0;
    while m < BCDIter do
        Update d_ij : d_ij = max(⟨t_j − t_i, v_ij⟩ / ||t_j − t_i||_2^2, 0);
        Update t_i : Solve a sparse, weighted, constrained linear least
        squares system of equations collected from (2) by Cholesky decomposition (see supp. material for more details);
        m = m + 1;
    end while
    Update W_ij: W_ij = φ(ε), where
        ε = (||(t_j − t_i)d_ij − v_ij||_2^2 + β||R_i^T R_j − R_ij||_2^2)^{1/2};
    n = n + 1;
end while
```

3.3. Why does Shapefit/kick outperform LUD?

Using the same geometric analysis, we are now ready to clarify why Shapefit/kick [9] outperforms LUD [20] (if run on the same problem instances), as reported in [9] and verified by our experiments. For ease of discussion, we present their respective formulations below.

LUD:

$$\min_{\substack{\boldsymbol{t}_i, i\in V;\\ d_{ij}, ij\in E}} \sum_{ij\in E} ||\boldsymbol{t}_j-\boldsymbol{t}_i-d_{ij}\boldsymbol{v}_{ij}||_2, \quad (4)$$
$$s.t. \quad \sum_{i\in V}\boldsymbol{t}_i = 0; d_{ij}\geq c, \forall ij\in E,$$

where d_{ij} is deemed as a relaxation of $\|\boldsymbol{t}_j-\boldsymbol{t}_i\|_2$.

Shapefit/kick:

$$\min_{\boldsymbol{t}_i, i\in V} \sum_{ij\in E} \|P_{\boldsymbol{v}_{ij}^\perp}(\boldsymbol{t}_j-\boldsymbol{t}_i)\|_2, \quad (5)$$
$$s.t. \quad \sum_{i\in V}\boldsymbol{t}_i = 0, \sum_{ij\in E}\langle \boldsymbol{t}_j-\boldsymbol{t}_i, \boldsymbol{v}_{ij}\rangle = 1,$$

where $P_{\boldsymbol{v}_{ij}^\perp}$ denotes the projection onto the orthogonal complement of the span of $\boldsymbol{v}_{ij}$.

To tease out the connection between these formulations, we replace the LUD's constraint $d_{ij}\geq c$, which is for removing scale ambiguity and preventing all cameras from collapsing to a single point (under such case the penalty cost vanishes), with the one used in Shapefit/kick, i.e. $\sum_{ij\in E}\langle \boldsymbol{t}_j-\boldsymbol{t}_i, \boldsymbol{v}_{ij}\rangle=1$. We claim that the resultant optimization problem, denoted as RevisedLUD, has exactly the same optimal solution as that of Shapefit/kick. To verify this, we note that removing the constraint $d_{ij}\geq c$ reduces d_{ij} to a completely free variable. Similar to the analysis for our formulation (2), for a set of estimates $\hat{\boldsymbol{t}}_i, \forall i\in V$, the optimal d_{ij} would be such that $d_{ij}\boldsymbol{v}_{ij}$ equals to the projection of $\hat{\boldsymbol{t}}_j-\hat{\boldsymbol{t}}_i$ onto the direction along $\boldsymbol{v}_{ij}$. It is immediately clear that the residual being minimized in RevisedLUD is $\|\boldsymbol{t}_j-\boldsymbol{t}_i\|_2\sin\theta_{ij}$ (Fig. 1(e)) for any θ_{ij}. It is also clear that $\|P_{\boldsymbol{v}_{ij}^\perp}(\boldsymbol{t}_j-\boldsymbol{t}_i)\|_2$ coincides with $\|\boldsymbol{t}_j-\boldsymbol{t}_i\|_2\sin\theta_{ij}$ and this establishes our claim. We note here that RevisedLUD can also be assisted by rotation when optimized with IRLS in Algo. 1 with small changes (e.g. step 4 becomes $d_{ij}=\langle \boldsymbol{t}_j-\boldsymbol{t}_i, \boldsymbol{v}_{ij}\rangle$). We will have occasion to use this later when a convex initialization for BATA is called for.

Given the above equivalence, we can restrict our attention to the sole difference between the two algorithms, namely in the constraints discussed above, with a view to elucidating the impact that different formulations of these constraints have on performance. First observe that while the constraint used in RevisedLUD fixes the overall scale to a constant value, the one in LUD, i.e. $d_{ij}\geq c$, only imposes a lower bound on the scale. We note that the latter is a weaker constraint, in the sense that while it prevents the collapsing of cameras all the way to a single point, it still allows a partial shrinking to occur, i.e. shrinking without respecting the overall global shape. To see the difference more explicitly, suppose we feed the optimal solution $\boldsymbol{t}^S$ obtained from the more strongly constrained (5) into (4). The solution space in (4) can be conceptually distinguished into two optimization regimes 1 and 2. Regime 1 admits solution of the form $\gamma\boldsymbol{t}^S$ where γ is a scale to be optimized together with d_{ij}'s. Clearly, the optimal solution in regime 1 is essentially identical to that of (5). However, it is generally not the optimal solution if we permit regime 2, which solves the original (4) without the $\gamma\boldsymbol{t}^S$ restriction. As a consequence, the total residual may be further reduced by adjusting the scale of each residual term individually without respecting the overall global shape. In particular, those $i-j$ terms representing large baselines often have larger residu-

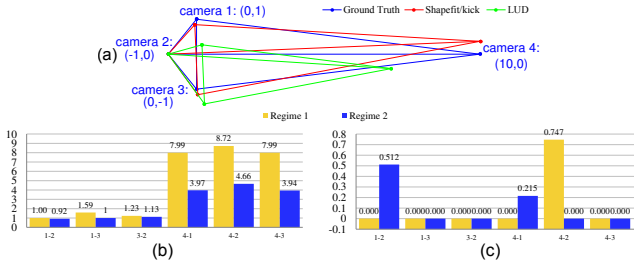

Figure 3: A toy example illustrating the squashing effect. (a) True and estimated camera locations (for better shape comparison, the three sets of camera configurations are aligned at camera 2 and normalized to have the same perimeter in the triangle formed by camera 1-3). (b)-(c) $\|\boldsymbol{t}_j - \boldsymbol{t}_i\|_2$ and $\|\boldsymbol{t}_j - \boldsymbol{t}_i - d_{ij}\boldsymbol{v}_{ij}\|_2$ plotted against $i-j$, which denotes the edge between camera i and j.

als as any slight deviation of the solution from the observation is scaled by the baseline magnitude. As the corresponding d_{ij}'s are less likely to have reached the lower bound c (since the optimal $d_{ij} = \min(\langle \hat{\boldsymbol{t}}_j - \hat{\boldsymbol{t}}_i, \boldsymbol{v}_{ij} \rangle, c)$ for the solution $\hat{\boldsymbol{t}}$), it thus pays to scale those larger baselines $||\boldsymbol{t}_j - \boldsymbol{t}_i||_2$ and d_{ij}'s down by shrinking camera i and j closer together as long as the reduction in residuals at these $i-j$ terms can more than make up for the increase in residuals in other terms. The best solution would therefore exhibit a partial shrinking effect, with the overall shape of the camera configuration squashed. We give a concrete toy example to illustrate how disparate baselines would exacerbate this tendency. For simplicity, let us look at a four-camera 2D case where the true camera locations are at (0, 1), (-1, 0), (0, -1) and (10, 0), and all their pairwise relative directions are observed with a 3° noise. We first visualize the solutions obtained from (4) and from (5) together with the ground truth in Fig. 3(a). As can be seen, the distant camera 4 gravitates significantly towards cameras 1-3 in the solution of (4). We also plot the pairwise camera distances and the residuals of the best solutions (with c=1) from regime 1 (optimized by linearly searching γ) and 2 in Fig. 3(b)&(c), respectively. Fig. 3(b) corroborates what we said above: compared to the solution of regime 1, regime 2 tends to pull those well-separated camera pairs closer together. Note that for those camera pairs that have short baselines, their corresponding d_{ij} has already reached the lower bound, and thus the $\boldsymbol{t}_i$ and $\boldsymbol{t}_j$ cannot shrink in tandem with those of the well-separated cameras without $\|\boldsymbol{t}_j - \boldsymbol{t}_i\|_2$ deviating too far from the d_{ij}, leading to squashing effect in the camera configuration. Referring to Fig. 3(c), first note that in this toy example the solutions of both regime 1 and 2 agree with most of the observations exactly; we attribute this to the fact that the objectives of (4) and (5) are actually based on a group-sparsity term [34, 18], i.e. $L_{2,1}$ norm, which favors sparse residuals. Note also that regime 2 achieves a lower total residual (0.727) compared to regime 1 (0.747) by suppressing the large residual (the lone yellow peak) at the expense of the small residuals, validating our analysis above.

This observation is generally useful and applicable to other methods where such lower bound exists (e.g. [16]), or latter works based on LUD framework (e.g. [22, 27]).

4. Experiments

4.1. Synthetic Data Experiments

We first study the performance of different methods on synthetic data. To synthesize the view graph, we first generate the ground-truth camera locations $\bar{\boldsymbol{t}}_i, \forall i \in V$, by drawing i.i.d. samples from $N(0, I_{3\times 3})$. Denoting the number of cameras as n (set as 200 here), the pairwise edges E are then drawn randomly from the Erdős-Rényi model $\mathcal{G}(n, p)$, meaning each edge is observed with probability p, independently of all other edges. We then perturb the observed pairwise directions to mimic the effect of noises and outliers. As opposed to [20, 9] where Gaussian noises are added to the endpoint of the direction vector followed by a normalization to be of unit norm, we directly add noise to the orientation of the pairwise direction; we believe this to be more reflective of the actual perturbation. Specifically, we obtain each corrupted pairwise direction $\boldsymbol{v}_{ij}$ as follows,

$$\boldsymbol{v}_{ij} = \begin{cases} \boldsymbol{v}^u_{ij}, & \text{with probability q,} \\ R(\sigma\theta^g_{ij}, \boldsymbol{h}^u_{ij}) \dfrac{\bar{\boldsymbol{t}}_j - \bar{\boldsymbol{t}}_i}{||\bar{\boldsymbol{t}}_j - \bar{\boldsymbol{t}}_i||}, & \text{otherwise;} \end{cases} \tag{6}$$

where $\boldsymbol{v}^u_{ij}$ and $\boldsymbol{h}^u_{ij}$ are i.i.d. unit random vectors drawn from uniform distribution on the unit sphere and the orthogonal complement of the span of $\frac{\bar{\boldsymbol{t}}_j - \bar{\boldsymbol{t}}_i}{\|\bar{\boldsymbol{t}}_j - \bar{\boldsymbol{t}}_i\|_2}$, respectively. θ^g_{ij} is drawn from i.i.d. $N(0, 1)$ and σ is a scale controlling the noise level. $R(\sigma\theta^g_{ij}, \boldsymbol{h}^u_{ij})$ is a rotation matrix around the aixs $\boldsymbol{h}^u_{ij}$ for an angle $\sigma\theta^g_{ij}$ (counter-clockwise). Like [20], we use the normalized root mean square error (NRMSE) to evaluate the accuracy: $NRMSE = \sqrt{\sum_{i\in V} \|\hat{\boldsymbol{t}}_i - \bar{\boldsymbol{t}}_i\|_2^2}$, where $\hat{\boldsymbol{t}}_i, \forall i \in V$ is the set of estimated locations. Both $\hat{\boldsymbol{t}}$ and $\bar{\boldsymbol{t}}$ are centralized and normalized, i.e. $\sum_{i\in V} \hat{\boldsymbol{t}}_i = \boldsymbol{0}$, $\sum_{i\in V} \|\hat{\boldsymbol{t}}_i\|_2^2 = 1$ and the same is true of $\bar{\boldsymbol{t}}$.

We compare the performance of different objectives including LUD [20], Shapefit/kick [9], the nonlinear objective from 1DSfM [32], and BATA. We follow 1DSfM to use Huber as the robust scheme for BATA. For 1DSfM and BATA, we evaluate both random initialization and initialization from RevisedLUD. In the latter, we run a few iterations (IRLSiter=10 & BCDiter=1) of naïve IRLS for RevisedLUD to bootstrap the 1DSfM and BATA (the results are denoted as "Con.Init.+1DSfM" and "Con.Init.+BATA"). We use Ceres [1] for the optimization of 1DSfM. LUD and Shapefit/kick are optimized by IRLS and ADMM. All methods are run until they are well converged (we fix the number of iterations for BATA as IRLSiter=20 & BCDiter=5).

We investigate the performance under six combinations of observation ratio p and outlier ratio q, each with increasing noise level σ, as shown in Fig. 4. The results are aver-

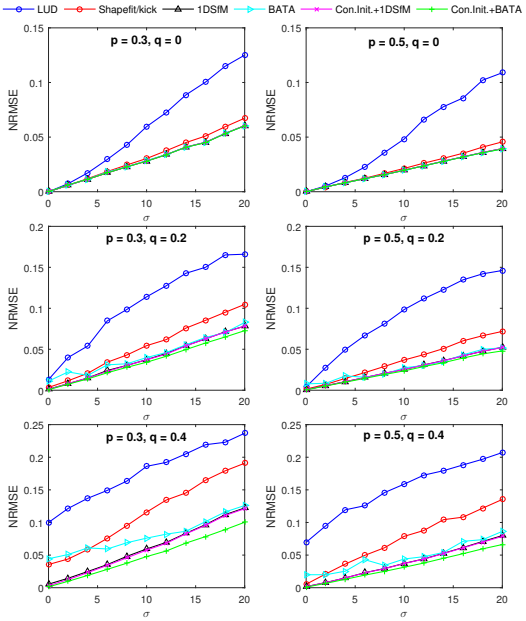

Figure 4: NRMSE from different methods under different view graph setup (p, q) and noise level σ.

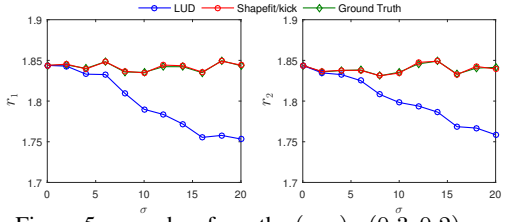

Figure 5: r_1 and r_2 from the (p, q)=$(0.3, 0.2)$ case.

aged over 20 independently generated view graphs. As we can see, angle-based objective functions generally achieve lower NRMSE compared to the magnitude-based counterparts. In particular, both 1DSfM and BATA can achieve better performance than LUD and Shapefit/kick even with random initialization, with the difference more notable under larger noises. Additionally, we observe that a good initialization is not important for 1DSfM here. We also observe that although 1DSfM and BATA tend to perform equally well in the outlier-free configurations, BATA, if bootstrapped with a good initialization, achieves higher accuracies when the camera configuration becomes increasingly ill-conditioned with lower p and higher q, e.g. the bottom-left case. We attribute this to the leveling off in the objective of BATA. Next, we demonstrate the partial shrinking bias caused by the lower-bound constraint in LUD. Under increasing noise, we monitor the following two ratios

$$r_1 = pct(\{S_{ij} | ij \in E\}, 75) / pct(\{S_{ij} | ij \in E\}, 25),$$

$$r_2 = pct(\{\|\boldsymbol{t}_i\|_2 | i \in V\}, 75) / pct(\{\|\boldsymbol{t}_i\|_2 | i \in V\}, 25),$$

to measure the extent of the partial shrinking bias, where $S_{ij} = \|\boldsymbol{t}_j - \boldsymbol{t}_i\|_2$ and $pct(\boldsymbol{a}, b)$ denotes the b-th percentile of $\boldsymbol{a}$. We plot the result for the (p, q)=$(0.3, 0)$ case in Fig. 5 and leave other cases to the *supp. material*. As can be seen,

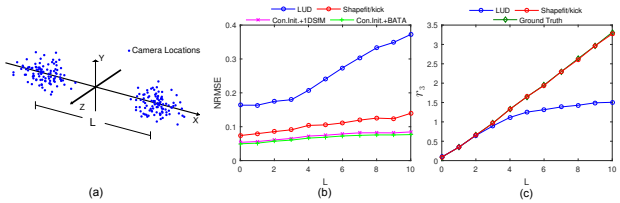

Figure 6: (a) Illustration of the two camera clusters. (b)-(c) NRMSE and r_3. Both are averaged over 20 trials.

compared to those in Shapefit/kick, both r_1 and r_2 in LUD become increasingly smaller than the ground truth under increasing noise level, indicating a squashing effect.

Finally, we test the sensitivity of the algorithms to an unbalanced distribution in the baseline magnitudes. For this purpose, the true camera locations are sampled from two separate clusters $N([-L/2, 0, 0], I_{3\times3})$ and $N([L/2, 0, 0], I_{3\times3})$, as illustrated by the dots in Fig. 6(a). The larger the L is, the more significant the unbalance in the baseline magnitudes is. We fix (p, q)=$(0.3, 0.2)$ and σ=10, and increase the value of L from 0 to 10. For each solution, we compute NRMSE[1] and the ratio $r_3 = l_{12}/(l_1 + l_2)$. l_{12} denotes the distance of the two cluster centers. l_1 and l_2 denote the median value of the set of distances from each point to their centers in the two clusters respectively. Note that r_3 explicitly measures the squashing effect caused by the different shrinking rates experienced by the longer inter-cluster baselines versus that of the shorter intra-cluster baselines. As shown in Fig. 6(b)-(c), under increasing L, the NRMSE's from the two magnitude-based methods, especially LUD, increase more significantly, meaning that they are more susceptible to the disparate baselines; it is also clear that r_3 from LUD decreases substantially compared to the ground truth, indicating a significant squashing effect.

4.2. Real Data Experiments

We now present the results on real unordered photo collections provided by the 1DSfM dataset [32] (see Fig. 7(a) for examples). The raw largest connected view graph released along with the dataset is used as our input. Similar to [32, 9, 6, 20], we apply the method of [4] to perform rotation averaging. To quantitatively evaluate the quality of a translation averaging estimate, it is compared with the gold standard output by Bundler [26]; the two sets of camera positions are robustly registered using the codes of [32].

We evaluate the performance of a few different setups under BATA to understand its behavior. The first case of interest is to simply run BATA from random initialization in two settings, without or with rotation involved in the IRLS re-weighting (denoted as "R.I. w/o R." and "R.I. w R."). Next, we use as initialization the moderately accurate output of a convex algorithm: to this end, we run a few rotation-

[1]Here, we centralize and normalize two clusters separately to avoid the inherent decreasing of NRMSE while increasing L.

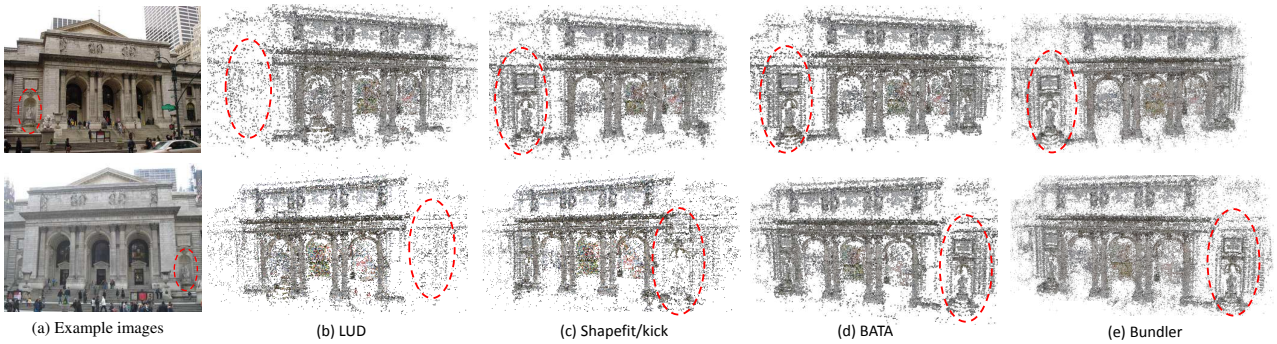

(a) Example images (b) LUD (c) Shapefit/kick (d) BATA (e) Bundler

Figure 7: Visualization of the point clouds after final BA on the NYC Library data. (a) depicts two images of the scene, with the red ellipses highlighting two sculptures. (b)-(e) show the resultant point clouds by the respective methods.

Data		1DSfM[32]		LUD[20]		Shapefit/kick[9]		Cui[6]		BATA													
										R.I. w/o R.			R.I. w R.			Con. Init.		w/o Rot.			w Rot.		
Name	N_c	$\tilde{e}$	$\bar{e}$	$\tilde{e}$	$\bar{e}$	$\tilde{e}$	$\bar{e}$	$\tilde{e}$	$\bar{e}$	$\tilde{e}$	$\bar{e}$	#iter	$\tilde{e}$	$\bar{e}$	#iter	$\tilde{e}$	$\bar{e}$	$\tilde{e}$	$\bar{e}$	#iter	$\tilde{e}$	$\bar{e}$	#iter
Piccadilly (PIC)	2508	1.4	6e3	-	-	1.2	15	1.3	2.5	4.3	13.8	100	1.5	7.5	78	3.0	5.0	1.0	5.2	100	**1.0**	4.2	57
Union Sq. (USQ)	930	5.0	2e3	-	-	8.9	47	5.5	12.7	7.2	15.4	100	6.3	14.9	100	6.2	11.9	4.3	12.4	100	**4.3**	12.3	100
Roman For. (ROF)	1134	3.2	2e4	-	-	4.3	25	2.9	9.4	3.2	24.2	100	2.4	23.7	100	9.4	20.8	1.6	9.9	100	**1.6**	16.3	88
Vienna Cath. (VNC)	918	2.1	3e4	5.4	10	**1.9**	11	2.7	5.9	2.5	18.2	100	2.0	16.5	77	6.1	13.1	1.9	12.1	99	**1.9**	13.3	74
Piazza Pop. (PDP)	354	3.0	54.2	**1.5**	5	3.6	5.9	2.0	2.7	2.1	11.0	100	1.9	8.9	96	1.4	6.5	1.7	6.7	100	4.2	6.2	62
NYC Library (NYC)	376	0.9	1e4	2.0	6	1.4	162	0.8	1.9	1.0	9.1	100	0.7	6.6	87	1.1	3.3	0.7	3.2	83	**0.6**	2.7	61
Alamo (ALM)	627	0.8	1e3	**0.4**	2	0.9	5.0	0.5	2.0	0.6	7.2	85	0.6	6.2	49	1.8	3.9	0.5	3.4	61	0.6	3.3	40
Metropolis (MDR)	394	3.8	6e4	**1.6**	4	6.0	81	2.7	10.6	3.6	34.1	100	2.1	24.5	85	4.5	15.7	4.0	15.3	97	1.8	12.1	64
Yorkminster (YKM)	458	1.7	1e4	2.7	5	-	-	2.3	5.7	1.2	15.9	100	1.0	15.2	98	4.4	12.8	1.3	8.4	100	**0.9**	8.0	85
Montreal N.D. (MND)	474	0.8	5e4	0.5	1	0.8	1.7	0.4	0.7	1.0	4.0	94	0.5	1.8	69	1.0	1.7	0.4	0.8	64	**0.3**	0.7	45
Tow. London (TOL)	508	3.1	6e3	4.7	20	2.3	164	**1.9**	11.2	2.5	25.2	100	2.3	18.5	99	5.1	22.9	2.1	13.5	100	2.2	16.0	100
Ellis Island (ELS)	247	1.8	9.8	-	-	1.9	12	2.5	5.5	1.6	22.5	97	1.5	15.8	53	2.2	9.7	1.4	11.1	80	**1.5**	13.4	39
Notre Dame (NOD)	553	**0.2**	1e3	0.3	0.8	**0.2**	1.5	**0.2**	0.6	0.4	5.7	100	0.2	4.5	76	3.1	4.1	0.3	1.8	96	**0.2**	2.1	70
Trafalgar (TFG)	5433	5.0	3e3	-	-	-	-	5.4	8.9	6.2	23.2	100	4.1	18.8	92	8.8	14.7	3.9	12.2	89	**3.4**	11.7	65

Table 1: Comparison of the accuracy of different methods in real data. N_c is the number of cameras in the view graph. $\tilde{e}$ and $\bar{e}$ respectively denote the median and mean distance error in meter unit. #iter denotes the number of outer iterations (the value of n in Algo. 1) required for convergence, bounded by 100. '-' indicates that the result is not available from the corresponding paper.

assisted IRLS iterations (IRLSiter=50 & BCDiter=1) of RevisedLUD (denoted as "Con. Init."). Again, BATA is run in the above two settings (denoted as "w/o Rot." and "w Rot."). We set IRLSIter=100 & BCDIter=5 with convergence condition being $|f^c - f^l|/f^l < 10^{-5}$, where f^l and f^c are the objective values of two consecutive iterations. All results are averaged over 20 trials.

We show these results in Tab. 1, together with those from four other state-of-the-art methods. Empirically We find BATA works well with a few different robust schemes, and here we only report the best results from Cauchy with α=0.1; other results (e.g. Huber) are given in *supp. material*. Since Shapefit/kick [9] provides multiple results with different combinations of preprocessing strategies, we only cite the overall best one. The errors are given in terms of median distance error $\tilde{e}$ and mean distance error $\bar{e}$ between the estimated and the reference camera locations. The median distance error is used as a main measurement of quality since it better captures the accuracy of the overall shape of camera locations. As can be seen, BATA obtains good accuracies even from random initialization. If bootstrapped by the convex method, the results generally improve. Compared to the naïve IRLS, the rotation-assisted IRLS generally improves the accuracies, especially in the case of random initialization. Also, "#iter" shows that it consistently reduces the number of iterations required for convergence. We now compare BATA's result from the "w Rot." case to those from the other four cited methods. The lowest median distance error is bolded for each scene. As can be seen, there is not one single best method for all the scenes. However, BATA gives the overall best performance in the sense that it achieves the lowest median distance errors $\tilde{e}$ in ten out of all the fourteen scenes. We note that the method of [6] generally achieves the lowest mean distance errors, which might be due to the local BA involved in their framework, making the estimation for those sparsely connected cameras less unstable. Also note that 1DSfM suffers from large mean errors. Next, we compare the ratio r_1 and r_2 computed from the LUD and Shapefit/kick result run on the raw view graph. As shown in Tab. 2, LUD generally returns a lower value of r_1 and r_2, indicating a squashing effect on the shape of the recovered camera locations. In view of the similarity of 1DSfM to BATA, we also test it on the raw view graph. We find that although it can recover those well-conditioned cameras well, BATA generally recovers those sparsely connected camera positions more reliably even with naïve IRLS. To show this, we plot the distribution of errors in the NYC Library scene in Fig. 8. As highlighted by the ellipses, BATA achieves higher accuracies on those cameras with relatively large errors and we find these cameras

Data	LUD		Shapefit/kick	
Name	r_1	r_2	r_1	r_2
PIC	2.26	2.43	2.71	2.81
USQ	2.27	2.60	6.54	3.08
ROF	2.54	2.19	4.62	2.57
VNC	2.42	2.85	2.73	2.63
PDP	2.48	2.57	2.87	2.33
NYC	2.33	2.22	2.69	2.34
ALM	2.24	2.65	2.55	2.82
MDR	2.28	2.22	6.95	10.2
YKM	2.46	2.24	3.21	2.86
MND	2.83	2.13	3.65	1.74
TOL	2.41	2.73	3.12	2.38
ELS	1.86	2.26	2.09	3.19
NOD	2.43	2.34	2.96	2.58
TFG	2.27	2.24	2.63	3.03

Table 2: Comparison of r_1 and r_2 from LUD and Shapefit/kick.

Data	1DSfM[32]			LUD[20]			Shapefit/kick[9]			Cui[6]			BATA		
Name	T_p	T_t	T_Σ	T_p	T_t	T_Σ	T_p	T_t	T_Σ	T_p	T_t	T_Σ	T_{ini}	T_t	T_Σ
PIC	122	366	488	-	-	-	424	40	464	207	121	328	52.9	60.6	113.5
USQ	20	75	95	-	-	-	24	3.7	27.7	35	6	41	2.5	7.5	10.0
ROF	40	135	175	-	-	-	52	9.5	61.5	99	32	131	8.1	20.9	29.0
VNC	60	144	204	265	255	520	66	8.2	74.2	102	15	117	12.6	17.2	29.8
PDP	9	35	44	18	35	53	4.6	1.9	6.5	40	3	43	2.0	2.2	4.2
NYC	13	54	67	18	57	75	8.6	2.2	10.8	34	4	38	1.7	2.1	3.8
ALM	29	73	102	96	186	282	16	11	27	67	11	78	11.1	13.0	24.1
MDR	8	20	28	13	27	40	6.9	2.4	9.3	27	4	31	2.0	2.4	4.4
YKM	18	93	111	33	51	84	-	-	-	41	5	46	2.4	6.3	8.7
MND	22	75	97	91	112	203	15	3.5	18.5	57	5	62	5.4	4.1	9.5
TOL	14	55	69	23	41	64	15	2.8	17.8	46	6	52	2.1	4.4	6.5
ELS	7	13	20	-	-	-	2.9	1.4	4.3	34	3	37	1.4	1.0	2.4
NOD	42	59	101	325	247	572	23	7.1	30.1	61	9	70	11.7	11.7	23.4
TFG	-	-	-	-	-	-	-	-	-	441	583	1024	168.9	389.1	558.0

Table 3: Comparison of running time in seconds. T_p, T_{ini}, T_t, and T_Σ respectively denote the preprocessing time, initialization time, translation averaging time, and total time.

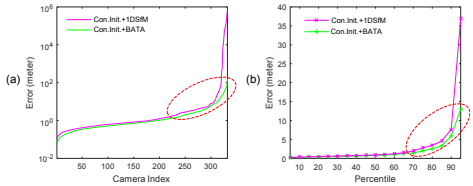

Figure 8: (a) Errors distribution (sorted in increasing order) for all cameras. (b) Errors in the 5th-95th percentile (50th percentile would be the median).

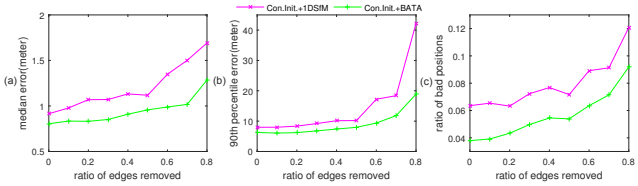

Figure 9: Different error quantities plotted against the ratio of the observed edges removed.

often have a smaller number of links to others. This seems to indicate that BATA is more superior in handling sparsely connected cameras. To corroborate this, we have tested their performance under increasingly sparser view graph by manually removing the observed edges. We plot the median error, the 90th percentile error and the ratio of cameras with large error (>20m, termed as bad positions) against the ratio of edges removed in Fig. 9. As we can see, although the difference in median error is small, (b)&(c) show that the two methods deviate from each other largely in their ability to localize those more "problematic" cameras, especially when the view graph becomes increasingly sparser and more cameras become sparsely connected. We leave more results from other scenes to the *supp. material*.

Next, we feed the initial poses obtained from different methods into a final BA step, using the Ceres[1]-based pipeline in Theia [27]. We present an example of the BA results on the NYC Library scene. We note that although different final BA schemes may give results of different qualities, adopting the same pipeline means that the results are only affected by, and thus indicate, the accuracy of the initial camera poses. We compare our result to that from the two magnitude-based methods. We use the implementation in [27] to obtain the camera pose estimates from the full pipeline of LUD method. The results of Shapefit/kick were provided by the authors. As shown in Fig. 7, although all the methods can reconstruct the main building reasonably well, not all can reconstruct the detailed structures of the two sculptures nearby. As highlighted by the red ellipses, LUD fails to recover both of them, and Shapefit/kick is able to recover only the left one while the point cloud of the right one is somewhat blurred and shifted. BATA can recover both of them successfully and yields the most similar results to those of the Bundler.

Finally, we compare the running time of different methods. Ours are obtained on a normal PC with a 3.4 GHz Intel Core i7 CPU and 16GB memory. The results are given in Tab. 3. T_p denotes the general preprocessing time, which may include outlier filtering and pairwise translation re-estimation to improve the input quality [32, 20, 9], or local depth estimation and local BA [6]. T_{ini} denotes the time for convex initialization in our method, T_t the time for solving the translation averaging optimization, and T_Σ the total time. As can be seen, since BATA directly processes the raw EG view graph and the sequence of sparse linear system of equations involved can be solved by highly efficient libraries, it is generally faster by several times.

5. Conclusion

In this paper, we advocate a return to angle-based objectives for translation averaging, proposing a simple yet effective bilinear formulation with a rotation-assisted IRLS scheme, achieving good empirical performance. This formulation also contributes to a better understanding of the behavior of the existing convex methods.

Acknowledgements. This work was partially supported by the Singapore PSF grant 1521200082 and the Singapore MOE Tier 1 grant R-252-000-637-112.

References

[1] S. Agarwal, K. Mierle, and Others. Ceres solver. http://ceres-solver.org.

[2] M. Arie-Nachimson, S. Z. Kovalsky, I. Kemelmacher-Shlizerman, A. Singer, and R. Basri. Global motion estimation from point matches. In *3DIMPVT*, 2012.

[3] F. Arrigoni, L. Magri, B. Rossi, P. Fragneto, and A. Fusiello. Robust absolute rotation estimation via low-rank and sparse matrix decomposition. In *3DV*, 2014.

[4] A. Chatterjee and V. Madhav Govindu. Efficient and robust large-scale rotation averaging. In *ICCV*, 2013.

[5] D. Crandall, A. Owens, N. Snavely, and D. Huttenlocher. Discrete-continuous optimization for large-scale structure from motion. In *CVPR*, 2011.

[6] Z. Cui and P. Tan. Global structure-from-motion by similarity averaging. In *ICCV*, 2015.

[7] O. Enqvist, F. Kahl, and C. Olsson. Non-sequential structure from motion. In *ICCV Workshops*, 2011.

[8] J. Fredriksson and C. Olsson. Simultaneous multiple rotation averaging using lagrangian duality. In *ACCV*, 2012.

[9] T. Goldstein, P. Hand, C. Lee, V. Voroninski, and S. Soatto. Shapefit and shapekick for robust, scalable structure from motion. In *ECCV*, 2016.

[10] V. M. Govindu. Combining two-view constraints for motion estimation. In *CVPR*, 2001.

[11] R. Hartley, J. Trumpf, Y. Dai, and H. Li. Rotation averaging. *International journal of computer vision*, 103(3):267–305, 2013.

[12] R. Hartley and A. Zisserman. *Multiple view geometry in computer vision*. Cambridge university press, 2003.

[13] N. Jiang, Z. Cui, and P. Tan. A global linear method for camera pose registration. In *ICCV*, 2013.

[14] F. Kahl. Multiple view geometry and the L_∞-norm. In *ICCV*, 2005.

[15] D. Martinec and T. Pajdla. Robust rotation and translation estimation in multiview reconstruction. In *CVPR*, 2007.

[16] P. Moulon, P. Monasse, and R. Marlet. Global fusion of relative motions for robust, accurate and scalable structure from motion. In *ICCV*, 2013.

[17] P. Moulon, P. Monasse, R. Perrot, and R. Marlet. Openmvg: Open multiple view geometry. In *International Workshop on Reproducible Research in Pattern Recognition*, pages 60–74. Springer, 2016.

[18] F. Nie, H. Huang, X. Cai, and C. H. Ding. Efficient and robust feature selection via joint $l_{2,1}$-norms minimization. In *NIPS*, 2010.

[19] C. Olsson and O. Enqvist. Stable structure from motion for unordered image collections. *Image Analysis*, pages 524–535, 2011.

[20] O. Ozyesil and A. Singer. Robust camera location estimation by convex programming. In *CVPR*, 2015.

[21] J. L. Schönberger and J.-M. Frahm. Structure-from-motion revisited. In *CVPR*, 2016.

[22] S. Sengupta, T. Amir, M. Galun, T. Goldstein, D. W. Jacobs, A. Singer, and R. Basri. A new rank constraint on multi-view fundamental matrices, and its application to camera location recovery. In *CVPR*, 2017.

[23] T. Shen, S. Zhu, T. Fang, R. Zhang, and L. Quan. Graph-based consistent matching for structure-from-motion. In *ECCV*, 2016.

[24] K. Sim and R. Hartley. Recovering camera motion using L_∞ minimization. In *CVPR*, 2006.

[25] S. Sinha, D. Steedly, and R. Szeliski. A multi-stage linear approach to structure from motion. In *ECCV Workshops*, 2010.

[26] N. Snavely, S. M. Seitz, and R. Szeliski. Photo tourism: exploring photo collections in 3d. In *ACM transactions on graphics (TOG)*, volume 25, pages 835–846. ACM, 2006.

[27] C. Sweeney. Theia multiview geometry library: Tutorial & reference. http://theia-sfm.org.

[28] C. Sweeney, T. Sattler, T. Hollerer, M. Turk, and M. Pollefeys. Optimizing the viewing graph for structure-from-motion. In *ICCV*, 2015.

[29] B. Triggs, P. F. McLauchlan, R. I. Hartley, and A. W. Fitzgibbon. Bundle adjustmenta modern synthesis. In *International workshop on vision algorithms*, pages 298–372. Springer, 1999.

[30] R. Tron and R. Vidal. Distributed 3-d localization of camera sensor networks from 2-d image measurements. *IEEE Transactions on Automatic Control*, 59(12):3325–3340, 2014.

[31] R. Tron, X. Zhou, and K. Daniilidis. A survey on rotation optimization in structure from motion. In *CVPR Workshops*, 2016.

[32] K. Wilson and N. Snavely. Robust global translations with 1dsfm. In *ECCV*, 2014.

[33] C. Wu et al. Visualsfm: A visual structure from motion system. 2011.

[34] M. Yuan and Y. Lin. Model selection and estimation in regression with grouped variables. *Journal of the Royal Statistical Society: Series B (Statistical Methodology)*, 68(1):49–67, 2006.

[35] C. Zach, M. Klopschitz, and M. Pollefeys. Disambiguating visual relations using loop constraints. In *CVPR*, 2010.